

The Most Massive White Dwarfs in the Solar Neighborhood

Mukremin Kilic¹, P. Bergeron², Simon Blouin³, A. Bédard²

¹*Homer L. Dodge Department of Physics and Astronomy, University of Oklahoma, 440 W. Brooks St., Norman, OK, 73019, USA*

²*Département de Physique, Université de Montréal, C.P. 6128, Succ. Centre-Ville, Montréal, QC H3C 3J7, Canada*

³*Los Alamos National Laboratory, P.O. Box 1663, Mail Stop P365, Los Alamos, NM 87545, USA*

Submitted 15 March 2021

ABSTRACT

We present an analysis of the most massive white dwarf candidates in the Montreal White Dwarf Database 100 pc sample. We identify 25 objects that would be more massive than $1.3 M_{\odot}$ if they had pure H atmospheres and CO cores, including two outliers with unusually high photometric mass estimates near the Chandrasekhar limit. We provide follow-up spectroscopy of these two white dwarfs and show that they are indeed significantly below this limit. We expand our model calculations for CO core white dwarfs up to $M = 1.334 M_{\odot}$, which corresponds to the high-density limit of our equation-of-state tables, $\rho = 10^9 \text{ g cm}^{-3}$. We find many objects close to this maximum mass of our CO core models. A significant fraction of ultramassive white dwarfs are predicted to form through binary mergers. Merger populations can reveal themselves through their kinematics, magnetism, or rapid rotation rates. We identify four outliers in transverse velocity, four likely magnetic white dwarfs (one of which is also an outlier in transverse velocity), and one with rapid rotation, indicating that at least 8 of the 25 ultramassive white dwarfs in our sample are likely merger products.

Key words: stars: evolution — white dwarfs

1 INTRODUCTION

Stellar evolution theory tells us that stars with initial masses less than about $8 M_{\odot}$ form degenerate cores and evolve into white dwarfs that are supported by electron degeneracy pressure. Chandrasekhar (1931) showed that there is an upper mass limit for a star that is supported by electron degeneracy pressure, which is roughly $1.4 M_{\odot}$. Takahashi et al. (2013) studied the evolution of the progenitors for electron capture supernovae, and found that when the mass interior to the helium burning shell reaches $1.367 M_{\odot}$, the ONe core collapses due to electron capture on ^{24}Mg and ^{20}Ne , leading to the formation of a neutron star (Miyaji et al. 1980; Nomoto 1987). Hence, single star evolution cannot produce white dwarfs more massive than $1.367 M_{\odot}$.

Population synthesis models demonstrate that a significant fraction of the massive white dwarfs above $1 M_{\odot}$ likely form through double white dwarf mergers (Temminck et al. 2020; Cheng et al. 2020). The mergers of two CO core white dwarfs may leave behind a single massive white dwarf if the remnant’s mass is below the Chandrasekhar limit (Schwab 2021, and references therein).

Ultramassive white dwarfs have been discovered serendipitously in surveys of nearby white dwarfs. GD 50 is the best example of an ultramassive white dwarf identified early on (Bergeron et al. 1992). Based on Gaia Data Release 2 photometry and astrometry (Gaia Collaboration et al. 2018), GD 50 is an $M = 1.28 \pm 0.08 M_{\odot}$ white dwarf only 31 pc away from the Sun and likely a member of the AB Doradus moving group (Gagné et al. 2018). Magnetic white dwarfs PG 1658+441 (Schmidt et al. 1992) and RE J0317–853 (Barstow et al. 1995; Ferrario et al. 1997), and the nearby DA white dwarf LHS 4033 (Dahn et al. 2004) are similar, with mass estimates around

$1.3 M_{\odot}$. Recent examples of ultramassive white dwarfs include the discoveries of a $1.28 M_{\odot}$ white dwarf in the open cluster M37 (Cummings et al. 2016), a rapidly rotating $\sim 1.33 M_{\odot}$ DBA white dwarf (Pshirkov et al. 2020), and a $1.14 M_{\odot}$ white dwarf with a mixed hydrogen-carbon atmosphere (Hollands et al. 2020).

The 40 pc white dwarf sample in the northern hemisphere includes three white dwarfs with $\log g \geq 9$ (McCleery et al. 2020). The most massive white dwarf in that sample is WD 1653+256 with $M = 1.285 \pm 0.003 M_{\odot}$. Kilic et al. (2020) performed a detailed model atmosphere analysis of the 100 pc white dwarf sample in the SDSS footprint. With a larger survey volume, they found white dwarfs with masses up to $1.36 M_{\odot}$. J1140+2322, with $T_{\text{eff}} = 11850 \pm 200$ K and $M = 1.358 \pm 0.022$, is the most massive white dwarf in that sample, though the more precise Gaia EDR3 parallax (Gaia Collaboration et al. 2020) indicates a slightly more distant and less massive white dwarf. Both mass estimates for WD 1653+256 and J1140+2322 assume a CO core.

To search for the most massive white dwarfs in the solar neighborhood, here we present a detailed model atmosphere analysis of the spectroscopically confirmed or candidate ultramassive white dwarfs in the Montreal White Dwarf Database 100 pc sample (MWDD, Dufour et al. 2017). We discuss the details of our selection of ultramassive white dwarfs, and present follow-up spectroscopy of two of the newly identified candidates in Section 2. We provide the details of our fitting method and new evolutionary calculations in Section 3. We present the model atmosphere analysis of each object in Section 4, and discuss the properties of the ultramassive white dwarf sample in Section 5, and conclude.

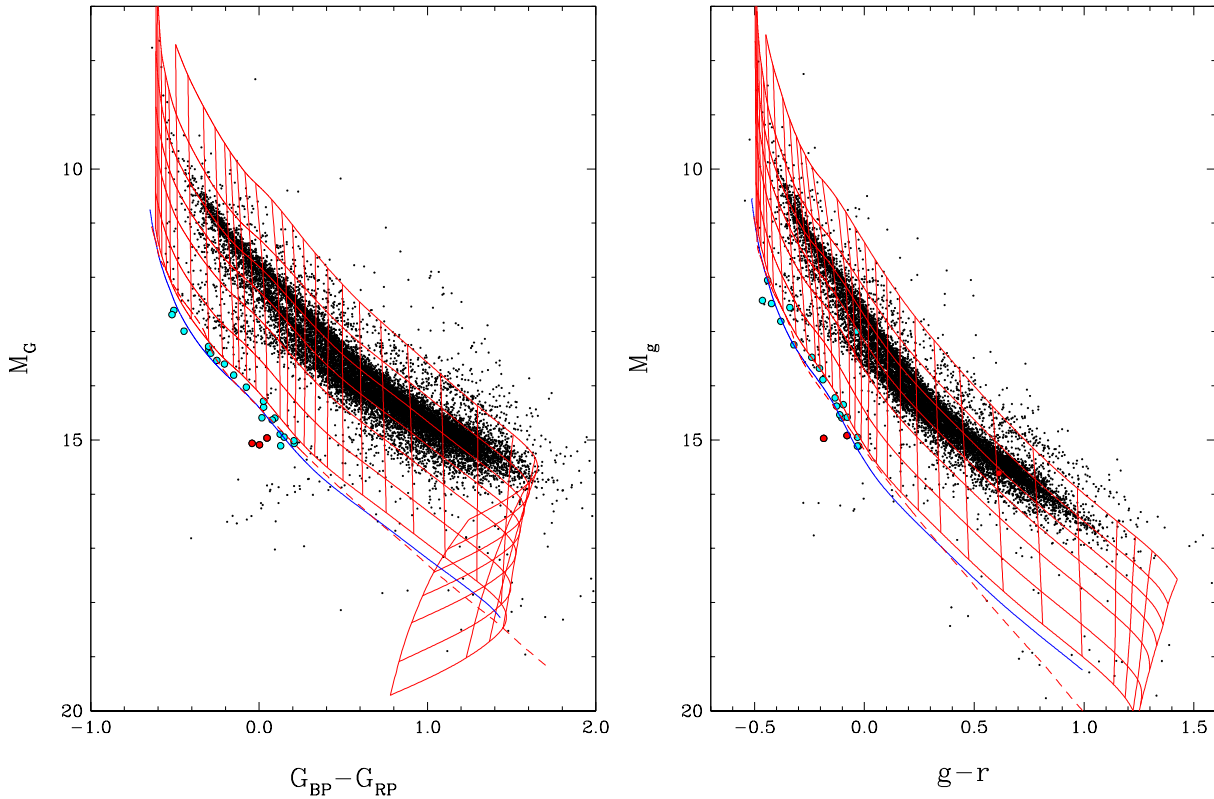


Figure 1. Gaia (left) and Pan-STARRS (right) color-magnitude diagram of the 100 pc sample in the Montreal White Dwarf Database (Dufour et al. 2017). Red solid lines show the cooling sequences for CO core and pure H atmosphere white dwarf models with 0.2, 0.4, 0.6, 0.8, 1.0, 1.2, and 1.3 M_{\odot} (from top to bottom). The dashed line shows the evolutionary sequence for 1.3 M_{\odot} pure He atmosphere white dwarfs, whereas the solid blue line shows the same for 1.29 M_{\odot} pure H atmosphere ONe core white dwarfs. Our ultramassive white dwarf sample and the three outliers are marked by filled cyan and red dots, respectively.

2 ULTRAMASSIVE WHITE DWARFS WITHIN 100 PC

2.1 Sample Selection

We use the 100 pc white dwarf sample from the MWDD to select ultramassive white dwarf candidates. The MWDD selection is based on Gaia DR2 (Gaia Collaboration et al. 2018), and includes all candidates with 10σ significant parallax (ϖ), G_{BP} and G_{RP} photometry, and $\varpi + \sigma_{\varpi} > 10$ mas. To create a clean sample, non-Gaussian outliers in color and absolute magnitude are removed using the recommendations from Lindegren et al. (2018), and a cut in Gaia color and absolute magnitude is used to select the white dwarf candidates¹.

Figure 1 shows the color-magnitude diagram of this sample in Gaia and Pan-STARRS (Chambers et al. 2016) filters, along with the evolutionary sequences for 0.2, 0.4, 0.6, 0.8, 1.0, 1.2, and 1.3 M_{\odot} (red lines, described further in section 3.3) CO core and 1.29 M_{\odot} ONe core (blue line, Camisassa et al. 2019) white dwarfs with pure H atmospheres. The dashed line shows the 1.3 M_{\odot} pure He atmosphere CO core white dwarf sequence. The main split in the white dwarf sequence due to the atmospheric composition (Bergeron et al. 2019), as well as the IR-faint (also referred to as ultracool) white dwarf sequence (Kilic et al. 2020), blue objects with $G_{BP} - G_{RP} \sim 0$ and $M_G \sim 16$ mag, are also clearly visible in this figure.

We use these color-magnitude diagrams to select ultramassive white dwarf candidates. Masses are estimated based on formal fits to the Gaia photometry and parallax. We restricted the candidates in

absolute magnitude ($M_G < 15.2$ mag) to avoid the IR-faint white dwarf sequence. The cyan symbols mark the candidates with $M > 1.3 M_{\odot}$ according to the full photometric fits assuming CO core models. We identify 23 ultramassive white dwarf candidates based on Gaia data. We repeat the same experiment using Pan-STARRS photometry (the right panel in Figure 1), and identify 22 candidates, 17 of which are common to both catalogs. Hence, we identify a total of 28 candidates for further analysis.

Strikingly, three stars in this sample (marked by red dots in Figure 1) seem to be significantly below the 1.29 M_{\odot} sequence for ONe core white dwarfs in the Gaia color-magnitude diagram (the left panel). This is suggestive of masses significantly above 1.3 M_{\odot} , and near the Chandrasekhar limit. For example, the most significant outlier in this figure, J0254+3019 (Gaia DR2 129352114170007680) would have $M = 1.414 \pm 0.032 M_{\odot}$ based on Gaia parallax and photometry and pure H atmosphere CO core white dwarf models. This object is also the most significant outlier in the Pan-STARRS color-magnitude diagram, but the Pan-STARRS photometry, which provides a broader wavelength coverage and improved constraints on the atmospheric parameters of our targets, indicates a slightly lower mass of 1.370 M_{\odot} for a pure H atmosphere white dwarf.

The Gaia EDR3 parallax for one of these three outliers, Gaia DR2 6033039719166862336, puts it well beyond 100 pc. In addition, its $G_{BP} - G_{RP}$ color in Gaia DR2 is significantly different than that in Gaia EDR3 and also the Pan-STARRS $g - r$ color. This object is marked by the red dot in the middle of the white dwarf sequence in the Pan-STARRS color-magnitude diagram shown in the right panel of Figure 1. We remove this object from the sample, as well as

¹ See <http://montrealwhitedwarfdatabase.org/faq.html> for details.

Table 1. Ultramassive White Dwarf Candidates.

| Object | Gaia DR2 Source ID | Gaia EDR3 ϖ (mas) | Gaia EDR3 μ (mas yr ⁻¹) | Gaia EDR3 V_{tan} (km s ⁻¹) | Gaia DR2 G (mag) | Gaia DR2 $G_{\text{BP}} - G_{\text{RP}}$ (mag) |
|--------------------------|-----------------------|-----------------------------|--|---|-----------------------|---|
| SDSS J114012.81+232204.7 | 3980865789203927680 | 13.77 ± 0.29 | 62.8 | 21.6 | 18.84 | +0.017 |
| SDSS J132926.04+254936.4 | 1448232907440917760 | 11.59 ± 0.10 | 23.6 | 9.7 | 17.69 | -0.446 |
| SDSS J172736.28+383116.9 | 1343557102670161664 | 9.76 ± 0.31 | 49.1 | 23.9 | 19.95 | +0.047 |
| SDSS J180001.21+451724.7 | 2115952197141317888 | 11.86 ± 0.10 | 72.4 | 29.0 | 18.22 | -0.206 |
| SDSS J221141.80+113604.5 | 2727596187657230592 | 14.52 ± 0.33 | 172.3 | 56.2 | 19.27 | +0.128 |
| SDSS J225513.48+071000.9 | 2712093451662656256 | 10.82 ± 0.37 | 45.0 | 19.7 | 19.22 | +0.036 |
| SDSS J235232.30-025309.2 | 2448933731627261824 | 33.35 ± 0.08 | 698.7 | 99.3 | 17.00 | +0.094 |
| WD J004917.14-252556.81 | 2345323551189913600 | 10.04 ± 0.25 | 36.2 | 17.1 | 19.07 | -0.076 |
| WD J010338.56-052251.96 | 2524879812959998592 | 34.42 ± 0.10 | 176.7 | 24.3 | 17.37 | +0.208 |
| WD J025431.45+301935.38 | 129352114170007680 | 10.16 ± 0.43 | 59.1 | 27.6 | 19.80 | +0.002 |
| WD J032900.79-212309.24 | 5099116118775025408 | 16.98 ± 0.24 | 71.1 | 19.9 | 18.84 | +0.149 |
| WD J042642.02-502555.21 | 4781653099991148928 | 12.74 ± 0.08 | 26.2 | 9.7 | 18.00 | -0.251 |
| WD J043952.72+454302.81 | 253936196167057664 | 10.43 ± 0.14 | 44.9 | 20.4 | 18.27 | -0.288 |
| WD J055631.17+130639.78 | 3343720447543820672 | 10.85 ± 0.53 | 58.3 | 25.5 | 19.73 | +0.207 |
| WD J060853.60-451533.03 | 5567732956694899712 | 11.62 ± 0.08 | 70.5 | 28.8 | 18.00 | -0.299 |
| WD J070753.00+561200.25 | 988421680189764224 | 11.52 ± 0.13 | 72.8 | 30.0 | 18.00 | -0.300 |
| WD J080502.93-170216.57 | 5721057173131773184 | 22.44 ± 0.10 | 426.7 | 90.1 | 17.64 | +0.027 |
| WD J093430.71-762614.48 | 5203792030921237248 | 11.85 ± 0.24 | 79.6 | 31.8 | 19.49 | +0.125 |
| WD J095933.33-182824.16 | 5671878015177884032 | 16.84 ± 0.15 | 104.6 | 29.4 | 18.17 | +0.026 |
| WD J111646.44-160329.42 | 3559695493657381248 | 15.52 ± 0.20 | 249.9 | 76.3 | 18.65 | +0.078 |
| WD J125428.86-045227.48 | 3678497445865946624 | 11.11 ± 0.26 | 9.8 | 4.2 | 18.60 | -0.151 |
| WD J174441.56-203549.05 | 4118923497232723072 | 10.05 ± 0.12 | 83.2 | 39.2 | 17.70 | -0.232 |
| WD J181913.36-120856.44 | 4153618204302689920 | 19.42 ± 0.07 | 11.5 | 2.8 | 15.77 | -0.483 |
| WD J183202.83+085636.24 | 4479342339285057408 | 13.24 ± 0.10 | 8.7 | 3.1 | 17.05 | -0.517 |
| WD J190132.74+145807.18 | 4506869128279648512 | 24.15 ± 0.05 | 119.8 | 23.5 | 15.70 | -0.507 |

two additional objects with incomplete (1 to 3 filter) Pan-STARRS photometry, lowering our sample size to 25 objects.

Table 1 presents the observational properties of this sample. We provide the SDSS object names, if available. Otherwise, we provide the object names in the WD J format as reported in the MWDD. We also provide the most recent astrometry from Gaia EDR3, but avoid using EDR3 photometry since the photometric calibration has changed between DR2 and EDR3. Our sample includes targets with Gaia G magnitudes ranging from 15.70 to 19.95 mag, with J0254+3019 and J1727+3831, the two remaining outliers highlighted in Figure 1, being the faintest.

2.2 Observations

We obtained follow-up optical spectroscopy of J0254+3019 and J1727+3831 using the 8m Gemini telescope equipped with the Gemini Multi-Object Spectrograph (GMOS) as part of the queue program GN-2020A-DD-113. We used the B600 grating and a 1'' slit, providing wavelength coverage from 3670 Å to 6855 Å and a resolution of 2 Å per pixel in the 4 × 4 binned mode. We obtained two 400s exposures of J0254+3019 and two 600s exposures of J1727+3831. We used the IRAF GMOS package to reduce these data.

Given the lack of any absorption lines in our relatively low signal-to-noise ratio spectrum of J0254+3019, we obtained four additional 826 s exposures as part of the program GN-2020B-FT-107. Our combined spectra from these two Gemini programs confirm the DC spectral type for J0254+3019 and DA type for J1727+3831.

3 MODEL ATMOSPHERE ANALYSIS

3.1 The Fitting Method

We use the photometric technique as described in Bergeron et al. (2019), and use the SDSS u and Pan-STARRS $grizy$ photometry along with the Gaia EDR3 parallaxes to constrain the effective temperature and the solid angle, $\pi(R/D)^2$, where R is the radius of the star and D is its distance. With a precise distance measurement from Gaia, we can constrain the radius of each star directly, and therefore its mass based on the evolutionary models for a given core composition.

The details of our fitting method, including the model grids used are further discussed in Bergeron et al. (2019), Genest-Beaulieu & Bergeron (2019), Blouin et al. (2019), and Kilic et al. (2020). Our model grids for both pure H and pure He atmosphere white dwarfs extend to $\log g = 9.5$. We supplement the pure H and pure He atmosphere model grids with mixed H/He atmosphere model grids with $\log \text{H/He} = -5$ for stars with temperatures below 12,000 K. Three of our targets are outside of the Pan-STARRS footprint; we use Gaia DR2 photometry in our analysis for those stars. Since all of our targets are within 100 pc, we do not correct for reddening.

3.2 The Core Composition

The unknown core composition is the biggest uncertainty in our analysis; the mass estimates are systematically lower for the ONe core model fits compared to the CO core fits. Murai et al. (1968) demonstrated that the transition from CO to ONe core composition in white dwarfs that evolve from single stars occurs at 1.06 M_{\odot} . Schwab (2021) studied the evolution of binary white dwarf merger remnants, and also found that the CO to ONe core transition occurs

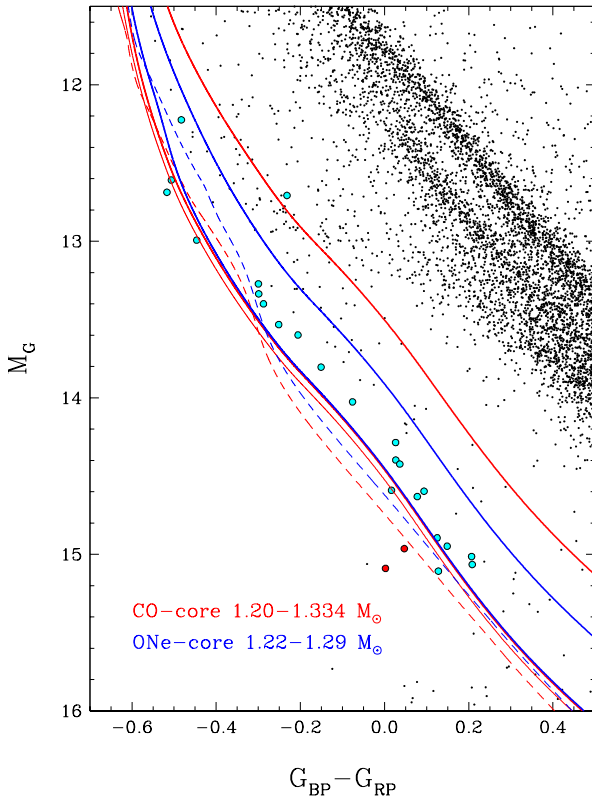


Figure 2. Color-magnitude diagram of the white dwarfs in the MWDD within 100 pc (colored symbols are discussed in the text) together with theoretical cooling sequences with CO (red) and ONe (blue) cores. The masses of the sequences are indicated in the figure; less massive sequences are more luminous. The most massive sequences for each core composition are shown for pure H (solid lines) and pure He (dashed lines) model atmospheres. Also displayed for the $1.334 M_{\odot}$, pure H atmospheres, CO core models, are the results for thick ($q_{\text{H}} = 10^{-4}$, thick red solid line) and thin ($q_{\text{H}} = 10^{-10}$, thin red solid line) H layers.

at a similar mass, $M \geq 1.05 M_{\odot}$, in single white dwarfs that formed via mergers.

Observationally, it is impossible to constrain the core composition of a given white dwarf and rule out massive CO core white dwarfs, unless they pulsate (e.g., [Giannichele et al. 2018](#)). However, [Cheng et al. \(2019\)](#) identify a significant cooling delay in high mass white dwarfs on the Q-branch ([Gaia Collaboration et al. 2018](#)). They suggest ^{22}Ne settling in CO core white dwarfs as a potential source of extra energy in these stars. [Bauer et al. \(2020\)](#) confirm that the location of the Q branch over-density in the Gaia color-magnitude diagram is compatible with CO cores, but not with ONe cores. This is based on the different crystallization temperatures of CO and ONe plasmas (see their Figure 3, and also Figure 2 from [Tremblay et al. 2019](#)). Ions in an ONe plasma have a higher charge, so they interact more strongly than those in a CO plasma and therefore freeze at a higher temperature. The location of the Q-branch over-density strongly favors CO cores even for white dwarfs more massive than $1.05 M_{\odot}$. Based on this, we adopt the CO core solutions in this study, but also present the ONe core solutions for comparison.

3.3 The Mass-Radius Relation

In our fits below, we use detailed mass-radius relations of CO core ($X_{\text{C}} = X_{\text{O}} = 0.5$) models ([Bédard et al. 2020](#)) with masses in the

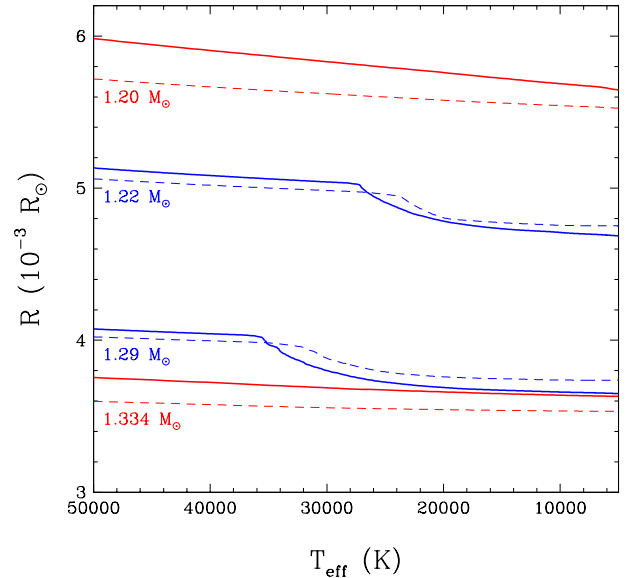


Figure 3. Stellar radius as a function of effective temperature for CO core (red line) and ONe core (blue line) white dwarf models with masses indicated in the figure. The solid and dashed lines correspond respectively to H-rich models ($q_{\text{H}} = 10^{-4}$ for CO core and $\sim 10^{-6}$ for ONe core models, respectively) and H-poor models ($q_{\text{H}} = 10^{-10}$ for CO core and no hydrogen for ONe core models, respectively).

range $M = 0.2 - 1.3 M_{\odot}$ by steps of $0.05 M_{\odot}$, and with thick ($q_{\text{H}} \equiv M_{\text{H}}/M_{\star} = 10^{-4}$) and thin ($q_{\text{H}} = 10^{-10}$) H layers to fit the H- and He-atmosphere white dwarfs in our sample, respectively. For the purpose of this analysis, we also calculated models at $M = 1.334 M_{\odot}$, which corresponds to the highest possible mass given the high-density limit of our equation-of-state tables ($\rho = 10^9 \text{ g cm}^{-3}$). We also rely on the ONe core, H-rich ($q_{\text{H}} \sim 10^{-6}$) and H-deficient ($q_{\text{H}} = 0$) models from [Camisassa et al. \(2019\)](#) at $M = 1.10, 1.16, 1.22,$ and $1.29 M_{\odot}$ to fit the H- and He-atmosphere white dwarfs, respectively.

We first consider the effects of core composition, stellar mass, surface composition, and thickness of the H layer on the predicted colors in the color-magnitude diagram. Figure 2 presents a zoomed-in version of the Gaia color-magnitude diagram previously displayed in Figure 1. Colored symbols mark our ultramassive white dwarf sample presented in Table 1, along with the two outliers shown as red points. Note that one of our Pan-STARRS selected targets, J1744–2035, appears redder than the $1.20 M_{\odot}$ cooling sequence based on Gaia DR2 photometry. However, improved constraints from Pan-STARRS photometry clearly indicate that this is an $M \sim 1.3 M_{\odot}$ white dwarf (see §4.4).

Figure 2 includes cooling sequences obtained from some of the CO and ONe core models discussed above (shown as red and blue lines, respectively). Calculations are shown for various masses indicated in the figure (less massive models are more luminous). Also shown for the most massive sequences are the results for pure H atmospheres (assuming thick H layers; solid lines) and for pure He atmospheres (assuming thin H layers for CO core models, or the H-deficient ONe core models from [Camisassa et al.](#); dashed lines); the small effect of using thick or thin H layers for pure H atmospheres is also illustrated for the CO-core models at $M = 1.334 M_{\odot}$ (thick and thin red solid lines, respectively). In this diagram, the CO and ONe core sequences for pure H atmospheres near $M \sim 1.2 M_{\odot}$ can be used to estimate the effects of the core composition, with the CO core models being more luminous due to their larger radii at a given effective temperature.

Interestingly enough, the CO-core sequence at $1.334 M_{\odot}$ overlaps almost perfectly with the ONe core sequence at $1.29 M_{\odot}$ in this color-magnitude diagram. However, the results for the pure He atmospheres for the same masses, which rely on the CO-core thin H models or the ONe core H deficient models, are quite distinct (note that colors calculated using CO core models with no hydrogen at all would overlap perfectly with our thin H models).

We can gain more insight into this behavior by examining the results displayed in Figure 3 where we show the stellar radius as a function of effective temperature for the same models illustrated in Figure 2, for both thick and thin H layers (or H deficient in the case of the ONe core models). For the $M \sim 1.2 M_{\odot}$ models, one can see the larger radii of the CO core models with respect to the ONe core models, as expected. The effect of the hydrogen layer mass at high temperatures is also consistent in both sets of models (the presence of hydrogen yields a larger radius at a given temperature); note that our CO-core models have hydrogen layers that are 100 times thicker than in the ONe core models. The effects of H in our CO core models are thus more pronounced. Also observed for the $M = 1.22$ and $1.29 M_{\odot}$ ONe core models is a drop in the stellar radius due to phase separation upon crystallization (see also Figure 11 of Camisassa et al. 2019). This drop in radius occurs at lower effective temperatures and with a smaller amplitude in H deficient models. The net result is that at lower temperatures, the H deficient ONe core models have larger radii than their thick H counterparts, in contrast with our CO-core models where phase separation is neglected. The effects are even more pronounced in the most massive CO-core and ONe core models displayed in Figure 3. Here the thick H layer, CO-core models at $1.334 M_{\odot}$ overlap almost perfectly with the ONe core models at $1.29 M_{\odot}$ below $T_{\text{eff}} \sim 30,000$ K, while the thin H (or H deficient) models yield stellar radii that differ significantly in the same temperature range, thus explaining the particular behavior observed in the color-magnitude diagram displayed in Figure 3 for the most massive sequences.

Finally, we note that both the CO-core and ONe core models are able to encompass most of the massive white dwarfs in our sample displayed in Figure 2, in particular if we take into account the effect of atmospheric composition. The only exceptions are the three red objects identified in the figure.

4 RESULTS

4.1 SDSS J172736.28+383116.9

Figure 4 shows our model fits to SDSS J172736.28+383116.9, hereafter J1727+3831, one of the outliers in the Gaia color-magnitude diagram. The Pan-STARRS photometry puts this object closer to the $1.3 M_{\odot}$ models (see Figure 1). The top panel shows the GALEX NUV, SDSS u , and Pan-STARRS $griz$ photometry (error bars) along with the predicted fluxes from the best-fitting pure H (filled dots) and mixed H/He (open circles) atmosphere models. The GALEX photometry is not used in the fitting, and is shown in red here and in the following figures, but it is useful for inferring the atmospheric composition in some cases. The labels in the same panel give the Gaia DR2 Source ID, object name, and the photometry used in the fitting. The bottom panel shows the observed Gemini spectrum (black line) along with the predicted spectrum based on the pure H solution. Note that we do not fit the spectroscopy data here. Instead, we simply overplot the predicted Balmer line profile (red line) from the photometric fit to see if a given spectrum is consistent with a pure H atmosphere composition.

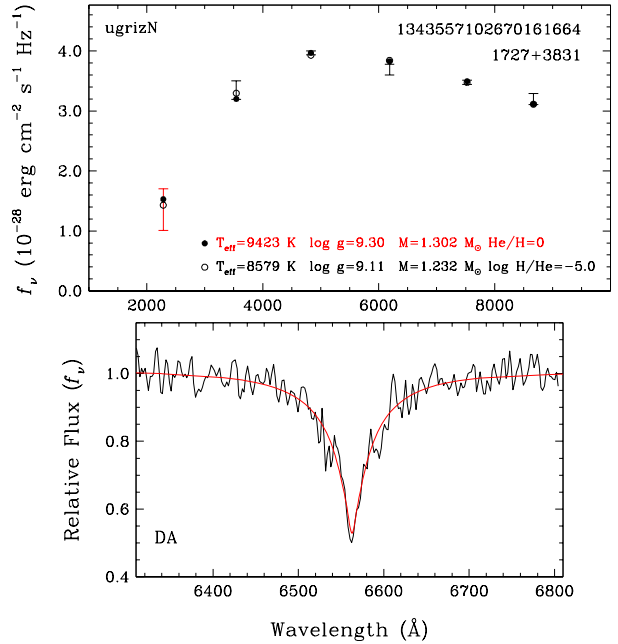


Figure 4. Model fits to an ultramassive white dwarf candidate observed at Gemini. The top panel shows the best-fitting H (filled dots) and He (open circles) atmosphere white dwarf models to the photometry (error bars), and includes the Gaia DR2 Source ID, object name, and the photometry used in the fitting: *ugrizN* means SDSS *u* + Pan-STARRS *griz*, and GALEX NUV. The atmospheric parameters of the favored solution is highlighted in red. Here, and in the following figures, we show the model parameters for CO core white dwarfs. The bottom panel shows the observed spectrum (black line) along with the predicted spectrum (red line) based on the pure H atmosphere solution.

We cannot distinguish between the H- or He-dominated solution for J1727+3831 based on the photometry alone. However, the observed Gemini spectrum is clearly that of a DA type star, and our photometric analysis indicates $T_{\text{eff}} = 9420 \pm 200$ K and $M = 1.302 \pm 0.011 M_{\odot}$ for a pure H atmosphere white dwarf with a CO core. The predicted H α line profile for these parameters provides an excellent match to the observed spectrum. Without additional information, there is no way to know the core composition. If J1727+3831 has an ONe core instead, its mass would be $0.05 M_{\odot}$ lower.

4.2 WD J025431.45+301935.38

Figure 5 shows our model fits to WD J025431.45+301935.38, hereafter J0254+3019, the most significant outlier in our sample. Even though Pan-STARRS photometry and Gaia EDR3 parallax indicate a mass as high as $1.37 M_{\odot}$ for a pure H composition, it turns out that J0254+3019 is a DC white dwarf with no visible absorption features in its spectrum. Hence, its atmosphere is clearly not dominated by H, and it appears to be an outlier in the color-magnitude diagrams because of its atmospheric composition.

He I lines disappear below about 11,000 K, which means that pure He atmosphere white dwarfs would appear as DC white dwarfs below this temperature. However, Bergeron et al. (2019) demonstrated that pure He atmosphere white dwarfs are extremely rare or nonexistent in the 6000 – 11,000 K temperature range. Reasonable mass estimates for DC white dwarfs in this temperature range require additional electron donors like hydrogen and carbon (or other metals). Given

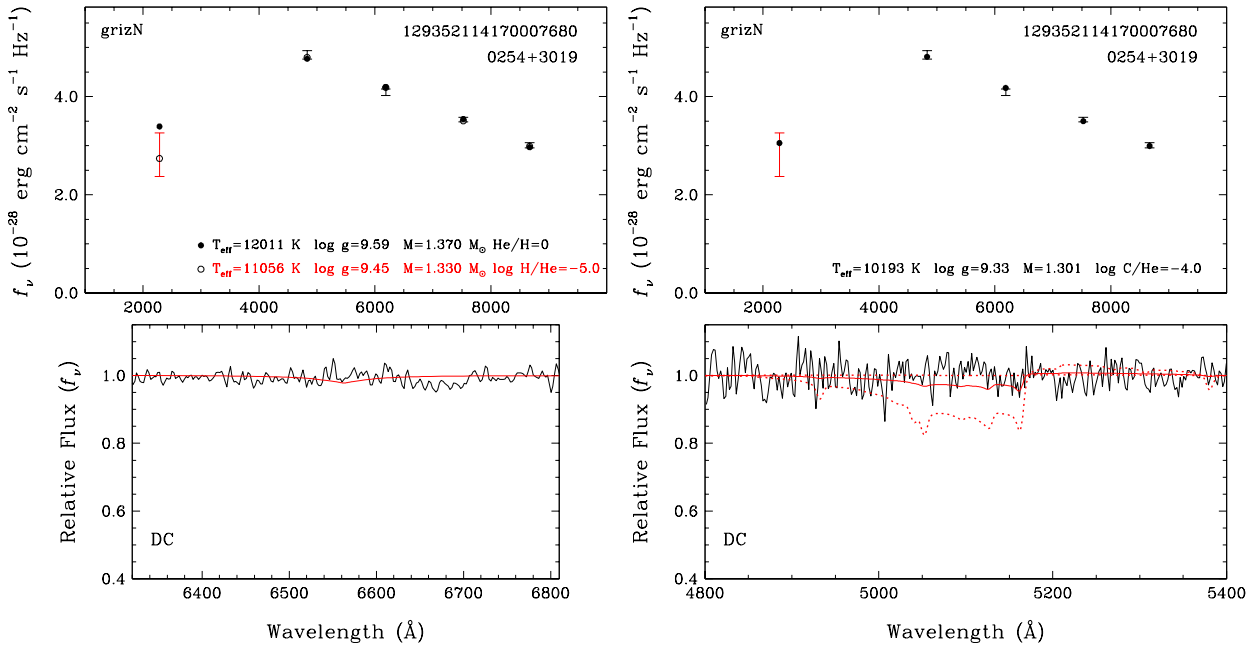


Figure 5. Model fits to J0254+3019, our second target observed at Gemini. The lack of any absorption features in its Gemini spectrum complicates our analysis of J0254+3019. The left panels show our analysis assuming pure H and He-rich models with trace amounts of H (similar to Figure 4), whereas the right panels show the results assuming a He-rich composition with trace amounts of C. In the lower panel, the red solid line corresponds to the model spectrum obtained from our photometric solution assuming a carbon abundance of $\log C/He = -4$, displayed in the upper panel, while the dotted lines show the predicted spectra assuming abundances of $\log C/He = -3$ and -5 . Depending on the unknown abundances of H and C in the atmosphere, J0254+3019 has a mass of 1.30-1.33 M_{\odot} , assuming a CO core.

the unknown atmospheric composition, we explore both possibilities for J0254+3019.

The left panels in Figure 5 show our model atmosphere analysis using pure H and mixed H/He models with $\log H/He = -5$. The top left panel shows our photometric fits, which indicate $T_{\text{eff}} = 11060 \pm 560$ K and $M = 1.330 \pm 0.016 M_{\odot}$ for a mixed H/He atmosphere and a CO core. The bottom left panel compares the predicted $H\alpha$ line profile for this solution to the observed spectrum. We can clearly rule out H abundances greater than this limit, as we would have detected an $H\alpha$ line. For an ONe core, the mass estimate goes down to 1.302 M_{\odot} .

The right panels in Figure 5 show the results from our analysis for a He atmosphere white dwarf with trace amounts of carbon. As discussed by Dufour et al. (2005), the physical parameters of DQ white dwarfs determined from the photometric method are particularly sensitive to the assumed carbon abundance. In particular, Figure 8 of Dufour et al. (2005) shows that the effective temperature and stellar mass can be significantly overestimated if pure He models are used instead of models that include carbon. In this case, the presence of carbon, in addition to producing strong atomic and molecular absorption features, also contributes to increase the number of free electrons, and thus the He^{-} free-free opacity, particularly in the continuum forming region, resulting in lower derived photometric temperatures. Since larger solid angles $-\pi(R/D)^2$ are required to fit the photometric data, this implies larger derived stellar radii or smaller masses. Note that a similar reasoning can be applied in the context of metal-rich DZ stars (see, e.g., Dufour et al. 2007), except at very low temperatures (Blouin et al. 2018).

Our photometric fits for J0254+3019, displayed in the right panels of Figure 5, using DQ models assuming various carbon abundances ($\log C/He = -5, -4$, and -3) are consistent with the picture de-

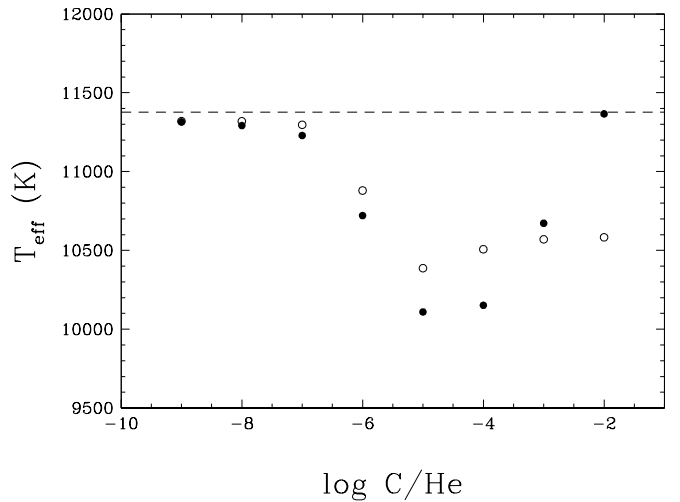


Figure 6. Effective temperature determined from photometric fits to J0254+3019 as a function of the assumed carbon abundance (filled circles). The dashed line indicates the temperature obtained from fits using pure He atmospheres. Similar results obtained using DQ model atmospheres where the carbon line and molecular opacities have been omitted are shown by open circles.

scribed above. Namely, the derived effective temperatures and stellar masses are always smaller than the values obtained from pure He models. However, our results also revealed that the lower the assumed carbon abundance (in the range explored here), the further away our solution was from the pure He solution! To understand this peculiar trend better, we computed additional models with a range

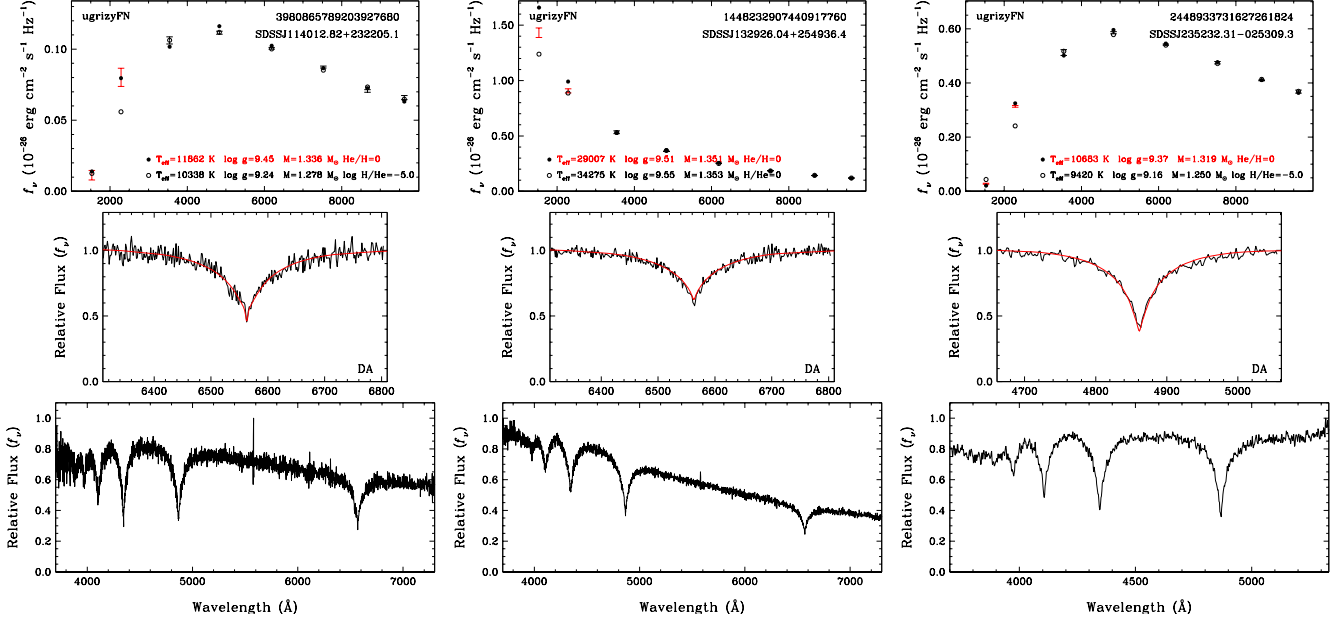


Figure 7. Model atmosphere fits to three ultramassive DA white dwarfs with spectroscopy available in the literature. The symbols and the panels are the same as in Figure 4, except that the bottom panels show a broader wavelength range for each object.

of carbon abundances, the results of which are displayed in Figure 6. By reducing further the carbon abundance below $\log C/He = -5$, we gradually recover the pure He solution. The molecular Swan bands are undetectable at $\log C/He = -5$ (see Figure 5), which implies that invisible traces of carbon can still have a large effect on the temperature structure, and thus on the derived physical parameters.

We attempted to isolate which of the effects produced by carbon — in terms of the equation-of-state or the opacity — account for the results displayed in Figure 6. For instance, we also show in Figure 6 (open circles) the results obtained from model atmospheres of DQ stars where the carbon line and molecular opacities have been turned off. While the difference in temperature between the $\log C/He = -5$ and -2 solutions has been significantly reduced, the derived photometric temperatures still show a non-monotonous variation as a function of the carbon abundance, indicating a complex interplay between the effects produced by carbon, both in terms of the equation-of-state and the opacity calculations.

The strongest carbon features are expected in the 5000–5200 Å range, and the lack of any significant features in our Gemini spectrum limits the carbon abundance to $\log C/He \leq -4$. If J0254+3019 has trace amounts of carbon in its atmosphere, then the best-fitting mass would be $1.301 \pm 0.014 M_{\odot}$ for a CO core, and $1.261 \pm 0.016 M_{\odot}$ for an ONe core. Hence, depending on the unknown atmospheric and core composition, J0254+3019 has a mass in the range 1.26 – 1.33 M_{\odot} .

Coutu et al. (2019) presented an analysis of the DQ white dwarfs in the MWDD, and showed that massive DQ white dwarfs hotter than 10,000 K have carbon abundances of $\log C/He > -4$. We can safely rule out such a carbon abundance in J0254+3019, and it is unlikely that J0254+3019 belongs to the massive DQ white dwarf population. Hence, the mixed H/He atmosphere solution discussed above is probably more representative of the physical parameters of this star.

4.3 Additional Targets with Follow-up Optical Spectroscopy

4.3.1 DA White Dwarfs

There are eight additional targets in our sample with follow-up spectroscopy available in the literature: four have spectra in the SDSS, and four others have spectra presented in Deacon et al. (2009, IPHAS J190132.77+145807.6), Gianninas et al. (2011, LHS 4033), Tremblay et al. (2020, G270-126), and Pshirkov et al. (2020, J1832+0856). These include 5 DA white dwarfs, two of which are magnetic, 1 DBA, and 2 DC white dwarfs.

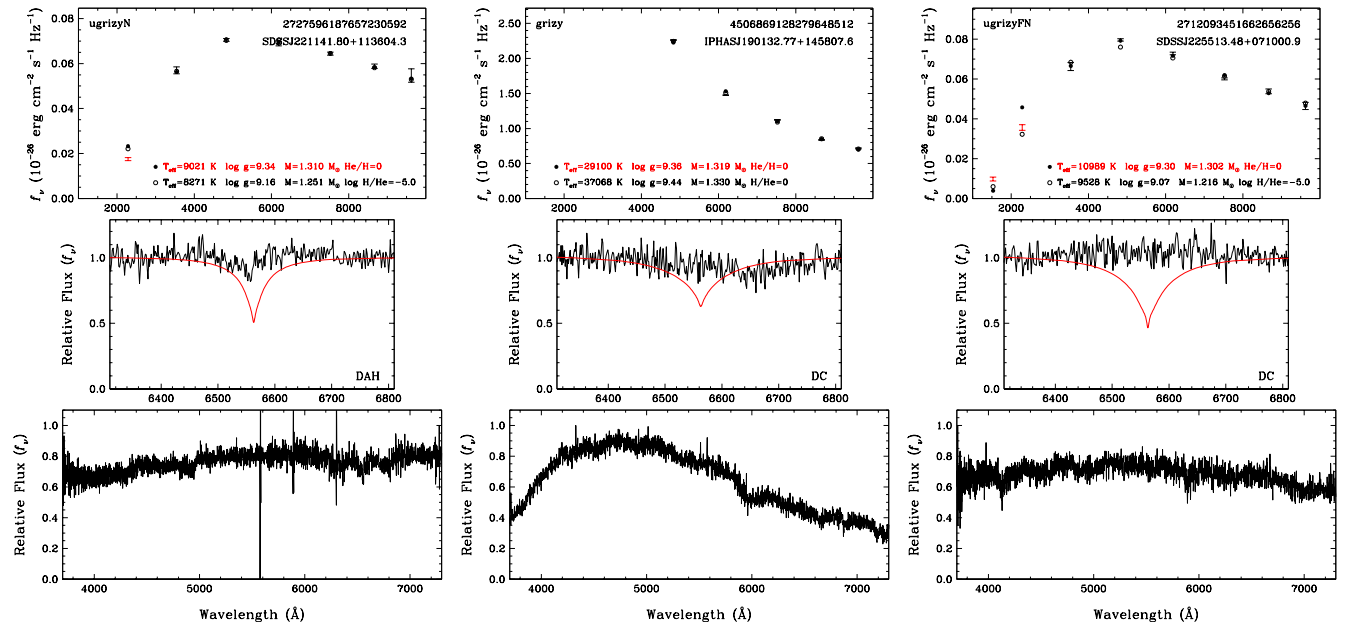
Figure 7 shows our model atmosphere analysis for the three non-magnetic DAs in our sample. The symbols and the panels are the same as in Figure 4, but we show an additional panel at the bottom to display a broader wavelength range for each object. These three stars have the entire set of Galex FUV and NUV, SDSS u , and Pan-STARRS *grizy* photometry available, which enable precise constraints on their temperatures, radii, and therefore masses. The photometric solutions provide an excellent match to the observed H line profiles, demonstrating that they have pure H atmospheres.

J2352–0253 (LHS 4033, the right panels) is one of the best studied ultramassive white dwarfs in the literature. Dahn et al. (2004) used both the photometric and spectroscopic method to demonstrate that this is an extremely massive white dwarf. They used the photometric technique with a ground-based parallax measurement from the USNO to derive $T_{\text{eff}} = 10,900 \pm 290$ K and $M = 1.31 - 1.33 M_{\odot}$, depending on the core composition. Dahn et al. (2004) had access to evolutionary models up to only 1.2 M_{\odot} , and they adopted the Hamada & Salpeter (1961) mass-radius relation for both the spectroscopic and photometric techniques. Hence, our analysis supersedes the results presented there. Nevertheless, our estimates of $T_{\text{eff}} = 10680 \pm 100$ K and $M = 1.319 \pm 0.003 M_{\odot}$ under the assumption of a CO core are entirely consistent with the results from Dahn et al. (2004).

The other DA white dwarfs in this figure, J1140+2322 and J1329+2549, are both hotter and more massive. The best-fitting mass estimates for CO cores are $M = 1.336 \pm 0.006 M_{\odot}$ and $1.351 \pm 0.006 M_{\odot}$, respectively. Both of these measurements are

Table 2. Physical Parameters of the Spectroscopy Sample assuming ONe or CO cores. All solutions above $1.29 M_{\odot}$ for ONe core models and above $1.334 M_{\odot}$ for CO core models are extrapolated.

| Object | Composition | Spectral Type | T_{eff} (K) | ONe core Mass (M_{\odot}) | ONe core Cooling Age (Gyr) | CO core Mass (M_{\odot}) | CO core Cooling Age (Gyr) |
|----------------------|-----------------|---------------|----------------------|-------------------------------|----------------------------|------------------------------|---------------------------|
| J010338.56–052251.96 | H | DAH: | 9040 ± 70 | 1.262 ± 0.003 | 2.84 ± 0.03 | 1.310 ± 0.003 | 2.60 ± 0.04 |
| J025431.45+301935.38 | log H/He = -5 | DC | 11060 ± 560 | 1.302 ± 0.024 | 2.25 ± 0.10 | 1.330 ± 0.016 | 1.49 ± 0.17 |
| ... | log C/He = -4 | DC | 10190 ± 290 | 1.261 ± 0.016 | 2.53 ± 0.08 | 1.301 ± 0.014 | 1.93 ± 0.12 |
| J114012.81+232204.7 | H | DA | 11860 ± 220 | 1.294 ± 0.008 | 2.10 ± 0.04 | 1.336 ± 0.006 | 1.71 ± 0.06 |
| J132926.04+254936.4 | H | DA | 29010 ± 750 | 1.314 ± 0.006 | 0.81 ± 0.05 | 1.351 ± 0.006 | 0.37 ± 0.03 |
| J172736.28+383116.9 | H | DA | 9420 ± 200 | 1.252 ± 0.012 | 2.78 ± 0.08 | 1.302 ± 0.011 | 2.59 ± 0.12 |
| J183202.83+085636.24 | He | DBA | 34210 ± 1020 | 1.301 ± 0.006 | 0.45 ± 0.03 | 1.319 ± 0.004 | 0.20 ± 0.02 |
| J190132.74+145807.18 | H | DC | 29100 ± 480 | 1.279 ± 0.003 | 0.61 ± 0.02 | 1.319 ± 0.004 | 0.35 ± 0.02 |
| ... | He | DC | 37070 ± 720 | 1.318 ± 0.004 | 0.40 ± 0.01 | 1.330 ± 0.003 | 0.14 ± 0.01 |
| J221141.80+113604.5 | H | DAH | 9020 ± 160 | 1.262 ± 0.009 | 2.85 ± 0.07 | 1.310 ± 0.008 | 2.61 ± 0.11 |
| J225513.48+071000.9 | H | DC | 10990 ± 210 | 1.252 ± 0.012 | 2.36 ± 0.05 | 1.302 ± 0.011 | 2.18 ± 0.09 |
| ... | log H/He = -5 | DC | 9530 ± 170 | 1.188 ± 0.014 | 2.88 ± 0.06 | 1.216 ± 0.018 | 2.48 ± 0.07 |
| J235232.30–025309.2 | H | DA | 10680 ± 100 | 1.272 ± 0.003 | 2.38 ± 0.02 | 1.319 ± 0.003 | 2.10 ± 0.03 |

**Figure 8.** Model atmosphere fits to three magnetic white dwarf candidates with spectroscopy available in the literature. The symbols and the panels are the same as in Figure 7. Note that J1901+1458 spectrum is not flux-calibrated.

above the highest mass CO core model available ($1.334 M_{\odot}$), and thus they are extrapolated and should be used with caution.

Table 2 presents the physical parameters of all 10 ultramassive white dwarfs with follow-up spectroscopy available, including these three DA white dwarfs. The best-fitting temperatures do not depend on the core composition, but the masses and the cooling ages do. For completeness, we provide the masses and the cooling ages for both ONe and CO core compositions in Table 2.

4.3.2 Magnetic White Dwarfs and Others

The left panels in Figure 8 show our model atmosphere analysis for the magnetic DA white dwarf J2211+1136, which shows a weak $H\alpha$ line. Since we do not model the magnetic field structure, our best-fitting pure H solution does not match the $H\alpha$ line profile. Regardless,

this is clearly a DA white dwarf, and our analysis indicates a mass of $1.310 \pm 0.008 M_{\odot}$ for a CO core.

IPHAS J190132.77+145807.6 (middle panels in Figure 8) was classified as a DC white dwarf by [Deacon et al. \(2009\)](#) since it does not show any significant features in its optical spectrum. However, it is too hot to be truly a DC white dwarf, as H or He lines should be visible at a surface temperature near 30,000 K. Hence, it must be a magnetic white dwarf, either a DAH or a DBH. Regardless of the atmospheric composition, J1901+1458 is clearly a very massive white dwarf with $M = 1.319 \pm 0.004 M_{\odot}$ (pure H solution) or $1.330 \pm 0.003 M_{\odot}$ (pure He solution) for a CO core.

Similarly, J2255+0710 (right panels) has a DC-like spectrum, but there are some weak features, including a broad unidentified absorption feature near 4130 Å. Hence, J2255+0710 is likely magnetic as well. Depending on the atmospheric composition, its mass is in the range $1.22\text{--}1.30 M_{\odot}$ for a CO core.

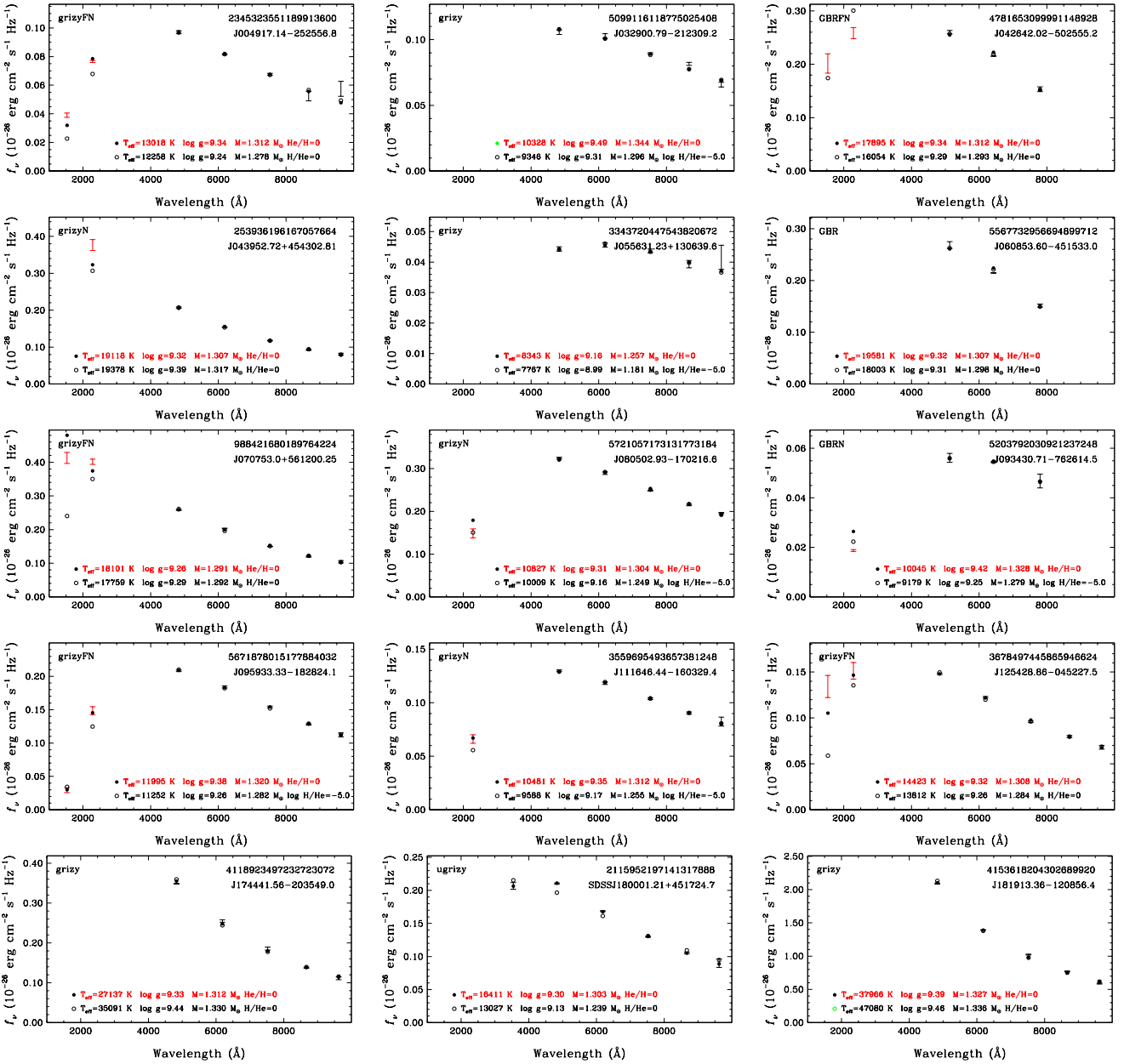


Figure 9. Model atmosphere fits to 15 ultramassive white dwarf candidates without follow-up spectroscopy. The symbols are the same as in Figure 4. The best-fitting parameters are for CO cores.

There are two additional targets with follow-up spectroscopy available in the literature. The first one, J0103-0522, is DAH: white dwarf included in the 40 pc sample of Tremblay et al. (2020). The remaining target, J1832+0856, is a rapidly rotating DBA white dwarf (Pshirkov et al. 2020). Our analysis using pure He atmosphere models for this object results in $T_{\text{eff}} = 34200 \pm 1020 \text{ K}$ and $M = 1.319 \pm 0.004 M_\odot$, assuming a CO core.

4.4 Objects with Unknown Spectral Types

Figure 9 shows the spectral energy distributions and our model atmosphere fits to 15 ultramassive white dwarfs with no follow-up spectroscopy available in the literature. Even though the presence or lack of a Balmer jump between the UV and optical filters can

be used to distinguish between the H- and He-atmosphere solutions, we refrain from assigning composition based on photometry alone. However, we note that there are several objects with spectral energy distributions that are best explained by H dominated atmospheres: J0049-2525, J0707+5612, J0959-1828, J1116-1603, J1254-0452, and J1800+4517 have SDSS u or GALEX UV data that clearly favor the pure H atmosphere solution. On the other hand, J0426-5025 and J0805-1702 have UV photometry that favor He-dominated atmospheres.

We provide both H- and He-dominated fits for each object in this figure, and list the best-fitting parameters for each composition in Table 3. All of these targets have $M \leq 1.344 M_\odot$ assuming CO core composition. Note that two objects, J0556+1306 and J0707+5612, have mass estimates below $1.3 M_\odot$ for the CO-core solutions. These two targets were selected as $M \geq 1.3 M_\odot$ white dwarfs based on Gaia

Table 3. Physical Parameters of the Photometry Only Sample assuming ONe or CO cores. All solutions above $1.29 M_{\odot}$ for ONe core models and above $1.334 M_{\odot}$ for CO core models are extrapolated..

| Object | Composition | T_{eff} (K) | ONe core Mass (M_{\odot}) | ONe core Cooling Age (Gyr) | CO core Mass (M_{\odot}) | CO core Cooling Age (Gyr) |
|----------------------|---------------|-------------------------|-------------------------------------|----------------------------------|------------------------------------|---------------------------------|
| J004917.14-252556.81 | H | 13020 ± 460 | 1.263 ± 0.011 | 1.94 ± 0.08 | 1.312 ± 0.010 | 1.72 ± 0.09 |
| ... | He | 12260 ± 390 | 1.236 ± 0.011 | 2.06 ± 0.08 | 1.278 ± 0.012 | 1.68 ± 0.07 |
| J032900.79-212309.24 | H | 10330 ± 290 | 1.305 ± 0.010 | 2.32 ± 0.06 | 1.344 ± 0.008 | 1.87 ± 0.09 |
| ... | log H/He = -5 | 9350 ± 250 | 1.256 ± 0.011 | 2.74 ± 0.07 | 1.296 ± 0.010 | 2.15 ± 0.10 |
| J042642.02-502555.21 | H | 17900 ± 1570 | 1.264 ± 0.019 | 1.30 ± 0.16 | 1.312 ± 0.016 | 1.08 ± 0.16 |
| ... | He | 16050 ± 1680 | 1.253 ± 0.031 | 1.51 ± 0.21 | 1.293 ± 0.028 | 1.15 ± 0.19 |
| J043952.72+454302.81 | H | 19120 ± 630 | 1.258 ± 0.008 | 1.18 ± 0.06 | 1.307 ± 0.007 | 0.96 ± 0.06 |
| ... | He | 19380 ± 1300 | 1.283 ± 0.019 | 1.24 ± 0.11 | 1.317 ± 0.014 | 0.81 ± 0.10 |
| J055631.17+130639.78 | H | 8340 ± 260 | 1.207 ± 0.021 | 3.33 ± 0.12 | 1.257 ± 0.023 | 3.34 ± 0.18 |
| ... | log H/He = -5 | 7770 ± 170 | 1.157 ± 0.029 | 3.53 ± 0.07 | 1.181 ± 0.029 | 3.33 ± 0.13 |
| J060853.60-451533.03 | H | 19580 ± 1910 | 1.258 ± 0.021 | 1.13 ± 0.16 | 1.307 ± 0.019 | 0.92 ± 0.17 |
| ... | He | 18000 ± 2800 | 1.259 ± 0.047 | 1.31 ± 0.29 | 1.298 ± 0.040 | 0.96 ± 0.26 |
| J070753.00+561200.25 | H | 18100 ± 350 | 1.240 ± 0.005 | 1.23 ± 0.04 | 1.291 ± 0.005 | 1.06 ± 0.04 |
| ... | He | 17760 ± 580 | 1.252 ± 0.009 | 1.31 ± 0.06 | 1.292 ± 0.009 | 0.98 ± 0.05 |
| J080502.93-170216.57 | H | 10830 ± 110 | 1.254 ± 0.004 | 2.40 ± 0.03 | 1.304 ± 0.003 | 2.20 ± 0.03 |
| ... | log H/He = -5 | 10010 ± 120 | 1.213 ± 0.004 | 2.70 ± 0.04 | 1.249 ± 0.006 | 2.23 ± 0.04 |
| J093430.71-762614.48 | H | 10050 ± 1350 | 1.284 ± 0.055 | 2.47 ± 0.35 | 1.328 ± 0.047 | 2.11 ± 0.50 |
| ... | log H/He = -5 | 9180 ± 1050 | 1.238 ± 0.052 | 2.86 ± 0.33 | 1.279 ± 0.051 | 2.32 ± 0.46 |
| J095933.33-182824.16 | H | 12000 ± 180 | 1.273 ± 0.005 | 2.12 ± 0.03 | 1.320 ± 0.004 | 1.83 ± 0.04 |
| ... | log H/He = -5 | 11250 ± 190 | 1.241 ± 0.007 | 2.31 ± 0.05 | 1.282 ± 0.007 | 1.85 ± 0.04 |
| J111646.44-160329.42 | H | 10480 ± 170 | 1.264 ± 0.007 | 2.45 ± 0.05 | 1.312 ± 0.006 | 2.21 ± 0.07 |
| ... | log H/He = -5 | 9590 ± 160 | 1.218 ± 0.007 | 2.82 ± 0.05 | 1.255 ± 0.010 | 2.33 ± 0.05 |
| J125428.86-045227.48 | H | 14420 ± 390 | 1.258 ± 0.008 | 1.71 ± 0.06 | 1.308 ± 0.007 | 1.52 ± 0.06 |
| ... | He | 13810 ± 310 | 1.243 ± 0.009 | 1.79 ± 0.05 | 1.284 ± 0.009 | 1.43 ± 0.04 |
| J174441.56-203549.05 | H | 27140 ± 890 | 1.271 ± 0.008 | 0.65 ± 0.06 | 1.312 ± 0.008 | 0.43 ± 0.04 |
| ... | He | 35090 ± 1410 | 1.317 ± 0.009 | 0.45 ± 0.05 | 1.330 ± 0.007 | 0.18 ± 0.03 |
| J180001.21+451724.7 | H | 16410 ± 290 | 1.253 ± 0.003 | 1.44 ± 0.03 | 1.303 ± 0.004 | 1.26 ± 0.04 |
| ... | He | 13030 ± 180 | 1.206 ± 0.004 | 1.85 ± 0.04 | 1.239 ± 0.006 | 1.57 ± 0.03 |
| J181913.36-120856.44 | H | 37970 ± 1940 | 1.305 ± 0.009 | 0.37 ± 0.03 | 1.327 ± 0.006 | 0.12 ± 0.03 |
| ... | He | 47080 ± 1000 | 1.327 ± 0.006 | 0.29 ± 0.01 | 1.336 ± 0.004 | 0.02 ± 0.01 |

photometry. However, our improved fits using Gaia EDR3 parallaxes and Pan-STARRS photometry indicate masses slightly below this limit.

5 DISCUSSION

5.1 The Most Massive White Dwarf in the Solar Neighborhood

By performing a detailed model atmosphere analysis of the MWDD 100 pc sample, we tried to identify the most massive white dwarfs in the solar neighborhood. Among the 10 objects with follow-up optical spectroscopy available, there are two objects with masses above $1.334 M_{\odot}$, the highest mass CO core model currently available. Hence, their mass estimates are extrapolated, and therefore uncertain. With that caveat in mind, the DA white dwarf J1329+2549 is currently the most massive white dwarf known in the solar neighborhood with well constrained atmospheric parameters and a mass of $1.351 \pm 0.006 M_{\odot}$.

Kilic et al. (2020) estimated a mass of $1.358 \pm 0.022 M_{\odot}$ for the DA white dwarf J1140+2322, which is also included in our sample. However, the previous analysis on this object was based on the Gaia DR2 parallax measurement and also limited to CO core models up to $1.2 M_{\odot}$. Based on evolutionary sequences extended up to $1.334 M_{\odot}$ and the Gaia EDR3 parallax measurement, which implies a slightly larger distance, we derive a mass of $1.336 \pm 0.006 M_{\odot}$ for J1140+2322, making it the second most massive white dwarf in our spectroscopy sample.

The MWDD sample selection is optimized for creating a clean white dwarf sample rather than completeness. Searching the Gaia DR2 white dwarf catalog of Gentile Fusillo et al. (2019) for $M \geq 1.3 M_{\odot}$ objects within 100 pc reveals 40 high probability candidates with masses up to $1.37 M_{\odot}$ under the assumption of a pure H atmosphere and a CO core. These mass estimates are based on Gaia DR2 photometry and parallaxes. Three of these systems did not make it into the clean candidate selection in the MWDD. Of the remaining 37 targets, 19 are included in our sample and in Table 1, but the remaining 18 are excluded because they appear less massive or because of our color and magnitude selection avoiding the IR-faint white dwarf sequence.

Among the 18 excluded objects, six have follow-up spectroscopy available in the literature. Three of these, Gaia DR2 2533306985471073920, 601566038739612160, 1358301480583401728, are in the SDSS footprint, and additional analysis by Kilic et al. (2020) using Gaia parallax and SDSS + Pan-STARRS photometry showed that their masses are below $1.3 M_{\odot}$. Another object, SDSS J071816.41+373139.1, could be included in our list of ultramassive white dwarfs if it has a He-dominated atmosphere. The best-fitting He-dominated atmosphere solution has $T_{\text{eff}} = 40636 \pm 1506$ K and $M = 1.316 \pm 0.008 M_{\odot}$ (Kilic et al. 2020). However, we do not expect to see a DC white dwarf at such a high temperature, unless it is a magnetic DBH or DAH; its atmospheric composition is uncertain. The pure H solution implies a mass below $1.3 M_{\odot}$. Hence, it is not surprising that it is excluded

from our list of 25 ultramassive white dwarfs presented in Table 1. Two additional objects, J1001+3903 and J1337+0001 (Harris et al. 2001; Gates et al. 2004), are spectroscopically confirmed IR-faint (ultracool) white dwarfs.

In summary, we are confident that we are not missing a large population of $M \geq 1.3 M_{\odot}$ ultramassive white dwarfs within the Gaia 100 pc sample. However, Gaia itself is missing a number of cool ultramassive white dwarfs, since such white dwarfs disappear quickly below Gaia’s $G = 20$ mag detection limit (Bergeron et al. 2019; Kilic et al. 2020).

5.2 Single Stars versus Mergers

A large fraction of the ultramassive white dwarfs in our sample have likely formed as a result of binary mergers. Based on population synthesis calculations, Temmink et al. (2020) suggest that around 30 to 50% of single white dwarfs with $M > 0.9 M_{\odot}$ form through a binary merger.

Merger populations can reveal themselves through their kinematics. Since merger systems would be found in older populations that are kinematically heated up, they should show a higher velocity dispersion compared to a population of single stars (Wegg & Phinney 2012). For example, studying the transverse velocity distribution of a large sample of $M = 0.8 - 1.3 M_{\odot}$ white dwarfs, Cheng et al. (2020) show that 20% of the massive white dwarfs in their sample must come from mergers. Similarly, Kilic et al. (2020) found that 10 of their 44 hot DA white dwarfs with $M > 1 M_{\odot}$ have transverse velocities in excess of 50 km s^{-1} , indicating a merger origin.

Figure 10 shows the Gaia colors and tangential velocities of our sample of 25 ultramassive white dwarfs presented in Table 1. Excluding the 3σ outliers, the average tangential velocity of the sample is $21 \pm 10 \text{ km s}^{-1}$, which is consistent with a young disk population. There are four objects with transverse velocities (see Table 1) that are significantly higher than expected, $> 50 \text{ km s}^{-1}$, for their cooling ages. These include the DA white dwarfs J2211+1136 (which is also magnetic) and J2352–0253 (LHS 4033), and two additional objects without follow-up spectroscopy, J0805–1702 and J1116–1603. Hence, these four ultramassive white dwarfs likely formed through mergers.

Merger populations can also reveal themselves through magnetism. A magnetic dynamo can be generated during a merger event though differential rotation within a common-envelope or an accretion disk (Briggs et al. 2015). Tout et al. (2008) suggest that all highly magnetic white dwarfs, either found as single stars or as components of magnetic cataclysmic variables, have a binary origin (but see Caiazzo et al. 2020). Briggs et al. (2015) further argue that binary mergers can explain both the observed incidence of magnetism and the mass distribution of highly magnetic white dwarfs.

Interestingly, out of the 10 ultramassive white dwarfs with follow-up spectroscopy, 4 are likely magnetic (see section 4.3.2). As discussed above, one of these stars, J2211+1136, also displays a large transverse velocity, further providing evidence for its merger origin.

Merger populations can also reveal themselves through rapid rotation. Modeling the evolution of the remnants of double white dwarf mergers, Schwab (2021) estimate rotation periods of 10–20 min for most remnants on the white dwarf cooling track. However, they find that the most massive white dwarfs with $M \geq 1.2 M_{\odot}$ likely have shorter rotation periods of 5–10 min.

Only one of the ultramassive white dwarf candidates in our sample has a rotation measurement available. Pshirkov et al. (2020) found a rotation period of 353 s for the DBA white dwarf J1832+0856, which is entirely consistent with the simulations by Schwab (2021).

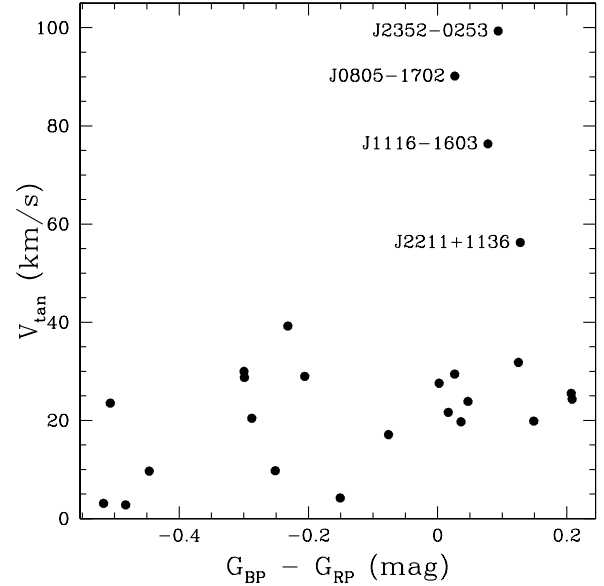


Figure 10. Gaia colors (from DR2) and tangential velocities (from EDR3) of our sample of ultramassive white dwarf candidates presented in Table 1. The four velocity outliers are labelled.

Hence, J1832+0856 has likely formed through binary evolution as well. Combining the results from these three different techniques shows that at least 8 of the 25 ultramassive white dwarfs in our sample are likely to have a binary origin.

5.3 Future Prospects

There are several factors that contribute to the rarity of ultramassive white dwarfs in the solar neighborhood. The steep slope of the initial-mass function (Salpeter 1955) means that their progenitor main-sequence stars are rare. In addition, given their smaller radii, ultramassive white dwarfs are fainter than average, hence harder to find in magnitude limited surveys. The latent heat from crystallization can keep these white dwarfs brighter for longer, but once they reach the Debye cooling regime, they cool rapidly and disappear from view. Their numbers are significantly depleted for ages older than a few Gyr.

Gaia DR2 has provided us with a sample of 25 ultramassive white dwarf candidates with $M \sim 1.3 M_{\odot}$ and within 100 pc. With increased precision in parallax and photometry, future Gaia data releases may reveal additional ultramassive white dwarfs in the solar neighborhood.

The Rubin Observatory’s 10-year Legacy Survey of Space and Time (LSST) will find millions of white dwarfs, which will include many ultramassive white dwarfs as well. An exciting prospect with these discoveries is that the time-series photometry from the LSST can be used to measure the rotation periods of ultramassive white dwarfs, and to identify rapidly rotating systems that likely formed through binary mergers. Such measurements can also constrain, as a function of mass, the fraction of single white dwarfs that form through mergers.

ACKNOWLEDGEMENTS

We acknowledge enlightening discussions with our late colleague G. Fontaine regarding the cooling sequences discussed in this work. MK thanks E. Baron for useful discussions.

This work is supported in part by the NSF under grant AST-1906379, the NSERC Canada, and by the Fund FRQ-NT (Québec). S.B. acknowledges support from the Laboratory Directed Research and Development program of Los Alamos National Laboratory under project number 20190624PRD2.

Based on observations obtained at the Gemini Observatory, which is operated by the Association of Universities for Research in Astronomy, Inc., under a cooperative agreement with the NSF on behalf of the Gemini partnership: the National Science Foundation (United States), National Research Council (Canada), CONICYT (Chile), Ministerio de Ciencia, Tecnología e Innovación Productiva (Argentina), Ministério da Ciência, Tecnologia e Inovação (Brazil), and Korea Astronomy and Space Science Institute (Republic of Korea).

DATA AVAILABILITY

The data underlying this article are available in the MWDD at <http://www.montrealwhitedwarfdatabase.org> and in the Gemini Observatory Archive at <https://archive.gemini.edu>, and can be accessed with the program numbers GN-2020A-DD-113 and GN-2020B-FT-107.

REFERENCES

- Barstow M. A., Jordan S., O’Donoghue D., Burleigh M. R., Napiwotzki R., Harrop-Allin M. K., 1995, *MNRAS*, **277**, 971
- Bauer E. B., Schwab J., Bildsten L., Cheng S., 2020, *ApJ*, **902**, 93
- Bédard A., Bergeron P., Brassard P., Fontaine G., 2020, *ApJ*, **901**, 93
- Bergeron P., Saffer R. A., Liebert J., 1992, *ApJ*, **394**, 228
- Bergeron P., Dufour P., Fontaine G., Coutu S., Blouin S., Genest-Beaulieu C., Bédard A., Rolland B., 2019, *ApJ*, **876**, 67
- Blouin S., Dufour P., Allard N. F., Kilic M., 2018, *ApJ*, **867**, 161
- Blouin S., Dufour P., Thibeault C., Allard N. F., 2019, *ApJ*, **878**, 63
- Briggs G. P., Ferrario L., Tout C. A., Wickramasinghe D. T., Hurley J. R., 2015, *MNRAS*, **447**, 1713
- Caiazzo I., et al., 2020, *ApJ*, **901**, L14
- Camisassa M. E., et al., 2019, *A&A*, **625**, A87
- Chambers K. C., et al., 2016, arXiv e-prints, p. arXiv:1612.05560
- Chandrasekhar S., 1931, *ApJ*, **74**, 81
- Cheng S., Cummings J. D., Ménard B., 2019, *ApJ*, **886**, 100
- Cheng S., Cummings J. D., Ménard B., Toonen S., 2020, *ApJ*, **891**, 160
- Coutu S., Dufour P., Bergeron P., Blouin S., Loranger E., Allard N. F., Dunlap B. H., 2019, *ApJ*, **885**, 74
- Cummings J. D., Kalirai J. S., Tremblay P. E., Ramirez-Ruiz E., Bergeron P., 2016, *ApJ*, **820**, L18
- Dahn C. C., Bergeron P., Liebert J., Harris H. C., Canzian B., Leggett S. K., Boudreault S., 2004, *ApJ*, **605**, 400
- Deacon N. R., et al., 2009, *MNRAS*, **397**, 1685
- Dufour P., Bergeron P., Fontaine G., 2005, *ApJ*, **627**, 404
- Dufour P., et al., 2007, *ApJ*, **663**, 1291
- Dufour P., Blouin S., Coutu S., Fortin-Archambault M., Thibeault C., Bergeron P., Fontaine G., 2017, in Tremblay P. E., Gaensicke B., Marsh T., eds, *Astronomical Society of the Pacific Conference Series Vol. 509*, 20th European White Dwarf Workshop. p. 3 (arXiv:1610.00986)
- Ferrario L., Vennes S., Wickramasinghe D. T., Bailey J. A., Christian D. J., 1997, *MNRAS*, **292**, 205
- Gagné J., Fontaine G., Simon A., Faherty J. K., 2018, *ApJ*, **861**, L13
- Gaia Collaboration et al., 2018, *A&A*, **616**, A10

- Gaia Collaboration Brown A. G. A., Vallenari A., Prusti T., de Bruijne J. H. J., Babusiaux C., Biermann M., 2020, arXiv e-prints, p. arXiv:2012.01533
- Gates E., et al., 2004, *ApJ*, **612**, L129
- Genest-Beaulieu C., Bergeron P., 2019, *ApJ*, **882**, 106
- Gentile Fusillo N. P., et al., 2019, *MNRAS*, **482**, 4570
- Giammichele N., et al., 2018, *Nature*, **554**, 73
- Gianninas A., Bergeron P., Ruiz M. T., 2011, *ApJ*, **743**, 138
- Hamada T., Salpeter E. E., 1961, *ApJ*, **134**, 683
- Harris H. C., et al., 2001, *ApJ*, **549**, L109
- Hollands M. A., et al., 2020, *Nature Astronomy*, **4**, 663
- Kilic M., Bergeron P., Kosakowski A., Brown W. R., Agüeros M. A., Blouin S., 2020, *ApJ*, **898**, 84
- Lindgren L., et al., 2018, *A&A*, **616**, A2
- McCleery J., et al., 2020, *MNRAS*, **499**, 1890
- Miyaji S., Nomoto K., Yokoi K., Sugimoto D., 1980, *PASJ*, **32**, 303
- Murai T., Sugimoto D., Hōshi R., Hayashi C., 1968, *Progress of Theoretical Physics*, **39**, 619
- Nomoto K., 1987, *ApJ*, **322**, 206
- Pshirkov M. S., et al., 2020, *MNRAS*, **499**, L21
- Salpeter E. E., 1955, *ApJ*, **121**, 161
- Schmidt G. D., Bergeron P., Liebert J., Saffer R. A., 1992, *ApJ*, **394**, 603
- Schwab J., 2021, *ApJ*, **906**, 53
- Takahashi K., Yoshida T., Umeda H., 2013, *ApJ*, **771**, 28
- Temmink K. D., Toonen S., Zapartas E., Justham S., Gänsicke B. T., 2020, *A&A*, **636**, A31
- Tout C. A., Wickramasinghe D. T., Liebert J., Ferrario L., Pringle J. E., 2008, *MNRAS*, **387**, 897
- Tremblay P. E., et al., 2019, *Nature*, **565**, 202
- Tremblay P. E., et al., 2020, *MNRAS*, **497**, 130
- Wegg C., Phinney E. S., 2012, *MNRAS*, **426**, 427

This paper has been typeset from a $\text{\TeX}/\text{\LaTeX}$ file prepared by the author.